Water Promotion (or Inhibition) of Condensation Reactions Depends on Exposed Cerium Oxide Catalyst Facets

Gengnan Li, Bin Wang, and Daniel E. Resasco*

Center for Interfacial Reaction Engineering

School of Chemical, Biological, and Materials Engineering

The University of Oklahoma

100 East Boyd St., Norman, OK 73019, USA

* Corresponding author (resasco@ou.edu)

Abstract

Nanoparticles with well-defined facets enable quantitative correlations between surface features and catalytic activity. Here, we explore the role of geometric and acid-base properties on the mechanism of aldol condensation catalyzed by ceria nanoshapes. In the crucial C–C coupling step, the two carbonyl adsorbates are bound to two adjacent cations. On the CeO_2 (110) plane, all atoms lie on the same layer, favoring the interaction between adsorbates and facilitating the bimolecular C–C coupling. Thus, the initial unimolecular deprotonation is rate limiting. By contrast, the (100) and (111) planes have an open structure with O on the top layer and Ce on the layer below. The former O layer interferes between adsorbates linked to Ce sites, making the C–C coupling rate limiting. Water helps overcoming this spatial hindrance by remote bond polarization via H-bonds. Therefore, water promotion is only observed on those planes for which the bimolecular step is rate limiting.

Keywords: Aldol condensation; Metal oxide, Nanoshapes, Acid-base; Kinetics; Geometric Effect; Water

Introduction

Metal oxides can effectively catalyze a wide variety of reactions of relevance in pharmaceutical and chemical industries,[1-2] sensors,[3-4] fuel cells,[5-8] and biomass conversion.[9-12] For example, C–C bond forming reactions, such as aldol condensation, represent a promising strategy for the production of fuels and chemicals from biomass,[10-20] particularly for distributed chemical manufacturing.[21] Recently, it has been shown that not only the acid-base properties, but also the geometry of the metal oxide surface may affect its reactivity.[22] Indeed, vapor phase condensation of C3 oxygenates on anatase TiO_2 occurs at higher rate than on the rutile form. It has been proposed that the stronger acidity and basicity of rutile TiO_2, as well as the longer length of the Ti-O bond on this surface inhibit the reprotonation and desorption of the dimer product, resulting in faster deactivation and overall lower activity of rutile compared to anatase. The reaction on rutile TiO_2 follows a second order kinetics with respect to the surface concentration. By contrast, on anatase the combination of a more suitable Ti-O distance and a moderate strength of the acid-base sites results in higher reactivity and stability. More interestingly, in this case the reaction is limited by the α-C–H abstraction, which results in a first-order kinetics with respect to the surface concentration of the ketone.

To better quantify differences like these, one would like to have catalysts with well-defined surface planes, such as those found on single crystals. Indeed, single-crystals have been used to study condensation reactions under ultra-high vacuum (UHV) conditions,[23-29] from which important correlations between catalytic performance and surface atomic arrangement have been obtained. In fact, it is highly desirable to use activity data from well-defined surfaces like those in single crystals to validate computational studies. However, it is always challenging to conduct conventional kinetics studies under realistic conditions on this type of low-surface-area model catalysts. Therefore, synthesizing high-surface-area catalysts with controlled shapes that expose different surface atom arrangements (facets) provides a unique opportunity to conduct comparative studies at high pressures, continuous flow rates and wide range of conversion, while still using well-defined surfaces. Such studies can become an effective tool for obtaining quantitative relationships between surface features and catalytic properties, such as selectivity, activity and rate of deactivation, which are not possible in UHV studies.

Among the metal oxide catalysts, cerium oxide (known as ceria, CeO_2) represents one of the most successful examples of materials design with controlled catalytic properties that are size- and shape-dependent. Among the most widely studied reactions catalyzed by ceria, redox processes in in emissions control[30-33] and acid-base catalyzed organic reactions[9, 34-37] have attracted the greatest attention. For example, Overbury et al.[38] have investigated the adsorption and reaction of acetaldehyde on various well-defined CeO_2 nanoshapes. Through hydrothermal synthesis, the CeO_2 nanoparticles with rod-like, cubic and octahedral morphology were found to mainly expose {110} + {100}, {100} and {111} facets, respectively. In situ FTIR indicates that the acidity of the Lewis sites (Ce cations) on these catalysts is weak, while the strength of the basicity depends on the topology of the terminated surfaces, due to the variety of defects such as oxygen vacancies and coordinative unsaturation of surface Ce and O ions. The strong basicity of nanorods (wires) and cubes compared to octahedra was found to favor activity for aldol condensation and Cannizzaro disproportionation reactions of acetaldehyde. Accordingly, the acetaldehyde conversion decreased in the order of basicity strength, i.e. nanorods (wires) > cubes > octahedra.

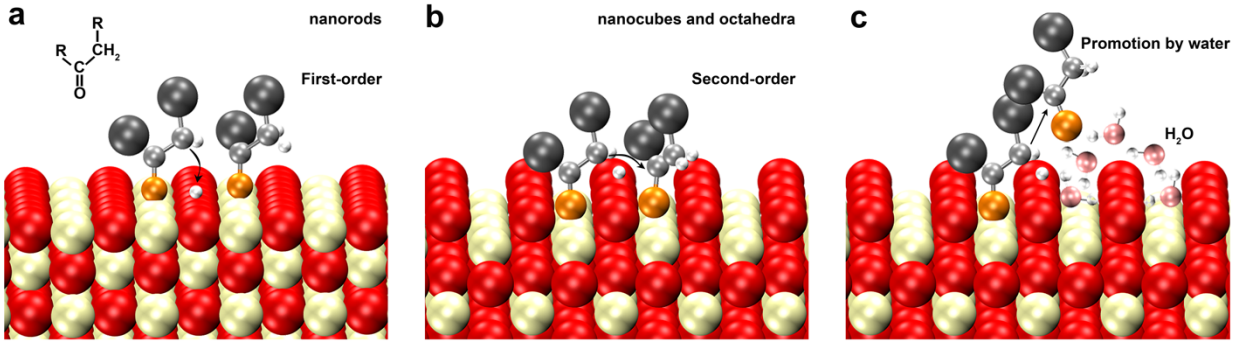

Figure 1. Schematic for the condensation paths on metal oxide surfaces with different atomic arrangement. (a**)** On a flat surface, C–C coupling is favorable, and the reaction is limited by α-C–H abstraction; (b) On a rough surface, reaction is limited by C–C bond formation; (c) The presence of water promotes C–C coupling on a rough surface. Red: O anions; Cream: Ce cations; Gray: generic R group; Silver: C; White: H; Orange: carbonyl O; Pink: O of H_2O molecule.

Water can affect catalytic activity or even change the reaction kinetics.[39] In previous studies, we have shown that the presence of water facilitates the bimolecular surface reaction by bridging cyclopentanone (CPO) molecules via remote bond polarization.[10, 14, 39] For example, on MCM-41-SO_3H with a low acid density, the sites are far enough apart to prevent direct cooperative dual-site

catalysis. In this case, water molecules can form a chain via H-bonds between the remote acid site and a CPO molecule near the enol species, making cooperative catalysis viable. As a result, in the presence of water, not only the rate increases, but also the reaction mechanism switches from single-site to dual-site.

Here, we have synthesized nanoparticles of CeO_2 following previously published synthesis procedures that have been successful employed to obtain structure-activity relationships.[38] By combining experimental kinetics and computational DFT calculations, we have explored the role of water on condensation reactions of ketone over different facets.[10, 14, 40] The intrinsic catalytic activity of these CeO_2 catalysts follows the trend nanorods > nanocubes > octahedra. Detailed kinetics assessment indicates that on nanorods the condensation rate is 1st order with respect to surface coverage and limited by α-C–H abstraction. Contrarily, on nanocubes and octahedra, it is 2nd order with respect to surface coverage and limited by the bimolecular C–C coupling.

As illustrated in **Figure 1**, the differences in reaction kinetics on the various CeO_2 nanoshapes can be interpreted in terms of geometric differences of the terminated surfaces. We propose that on CeO_2, water can extend the cooperative effect of neighboring sites overcoming the interference of surface O atoms, when the rate is limited by C–C coupling. Therefore, small amounts of water should cause activity enhancement on CeO_2 nanocubes and octahedra, but not on CeO_2 nanorods, for which the rate limiting step is not bimolecular.

Experimental Methods

Chemicals

Cerium (III) nitrate hexahydrate ($Ce(NO_3)_3 \cdot 6H_2O$, 99%), Sodium hydroxide (NaOH, 97%), anhydrous toluene (99.8%), cyclohexane (for HPLC, ≥ 99.9%), propionic acid (≥ 99.5%) and pyridine (> 99.9%) were purchased from Sigma-Aldrich and used without further treatment. Cyclopentanone (≥ 99%) was also purchased from Sigma-Aldrich and distilled before used as reactant. Deionized water (> 18.2 MΩ·cm) was used in every experiment.

Materials Synthesis

Cerium oxide (CeO_2) nanoparticles with different shapes were synthesized by a hydrothermal method conducted at different temperatures, following Overbury et al. [38, 41] Briefly, for CeO_2

nanorods, 0.434 g $Ce(NO_3)_3 \cdot 6H_2O$ and 4.8 g NaOH were dissolved in 2.5 mL and 17.5 mL water, respectively. Then, the $Ce(NO_3)_3.6H_2O$ solution was added at room temperature into the NaOH solution under stirring; additional stirring for 30 min resulted in the formation of a slurry. The mixture was then transferred into a 50-mL Teflon-lined stainless-steel autoclave and treated at 90 ˚C for 24 h. For the synthesis of CeO_2 nanocubes, the amount of $Ce(NO_3)_3 \cdot 6H_2O$ and NaOH used was the same as that for nanorods. However, the hydrothermal treatment temperature was raised to 180 ˚C for 24 h. Finally, for the CeO_2 octahedra, the amount of $Ce(NO_3)_3 \cdot 6H_2O$ was kept at 0.434 g but the NaOH was dropped to 0.008 g.[42] The hydrothermal treatment temperature and time were 180 ˚C and 24 h, the same as those for nanocubes. The resulting precipitates were collected by centrifugation, washed thoroughly with deionized water and dried under vacuum at 80 ˚C overnight, followed by a calcination process in tube furnace at 400 ˚C for 4 h in air with a heating ramp rate of 1.0 ˚C/min.

To prepare the CeO_2 nanocubes without Na, the solids obtained from the hydrothermal synthesis were further dispersed in 2.0 mL of 0.1 M NH_4OH solution under ultrasonic treatment for 5 min. After washing with hot water, the product isolated via centrifugation was then dispersed into 2.0 mL 0.1 M HNO_3 solution. The resulting suspension was placed in an ultrasonic bath for 5 min and the thus obtained Na-free CeO_2 nanocubes were collected via centrifugation after washing with hot water and drying in vacuum at 80 ˚C overnight. Finally, the products were subject to calcination at 400 ˚C for 4 h in air with a heating ramp rate of 1.0 ˚C/min.

Sample Characterization

Wide angle powder X-ray diffraction (PXRD) was performed on a Rigaku Ultima IV diffractometer (Cu Kα radiation, λ = 1.5406 Å) with Bragg-Brentano geometry in the 5–85 diffraction range, using a 0.01°step size under operating 40 kV voltage and 44 mA current, respectively. Nitrogen adsorption/desorption experiments were carried out on a ASAP 2020 adsorption system at -196 ºC. The samples were degassed at 200 ºC for 10 h under vacuum condition before measurement. The Brunauer-Emett-Teller (BET) method were employed to determine the catalyst surface area. Transmission electron microscopy (TEM) images were obtained using a JEOL JEM-2100 (JEOL Ltd., MA) transmission electron microscope, operating with an accelerating voltage of 200 kV and equipped with LaB_6 gun. The basicity of catalysts was characterized by temperature-programmed desorption of adsorbed CO_2 (CO_2-TPD). Before

measurement, 100 mg catalyst was pretreated at 200 ºC to remove the physisorbed species with a heating ramp rate of 10 ºC/min under 30 mL/min He flow. After cooling down to room temperature, the catalyst was exposed to a flow of CO_2 (30 mL/min) for 30 mins, followed by 2 hours He flow for removal of physisorbed CO_2. Finally, the desorption measurement was carried out in the temperature range of 25-900 ºC at a heating ramp rate of 10 ºC/min under 30 mL/min He flow. XPS (X-ray photoelectron spectroscopy) signals were collected on a Thermo Fisher ESCALAB 250XI instrument using monochromatic Al Kα X-rays at 1486.6 eV and 200 W power. All the elemental binding energies were referenced to the C (1s), 284.6 eV, used as internal reference.

Catalytic measurements

Reaction operating conditions. Aldol condensation of cyclopentanone (CPO) was performed in a 50 mL Mini Bench Top Parr high-pressure reactor (Model: 4592) equipped with a Parr 4848 Reactor Controller. In each run, 50 mg of catalyst was dispersed into the cyclohexane solvent and place in the reactor vessel. The system was purged with N_2 for three times to remove air inside. Then, the pressure was raised to 200 psig in N_2 and the temperature increased to 200 ºC while stirring at 500 rpm. After stabilization, the cyclopentanone reactant and the internal standard (toluene) were placed into a 30 mL feed cylinder, pressurized to 500 psig and injected into the reactor to ensure an accurately determined zero-time for the start of the reaction period. The initial CPO concentration was varied in each run to study the reaction kinetics. The total volume of liquid was kept constant (25 mL) in each run. After reaction, the product mixture was identified on a Shimadzu QP2010S gas chromatograph/mass spectrometer (GC-MS) and quantified on an Agilent 6890 gas chromatograph, equipped with flame ionization detector (GC-FID).

Effect of water on catalytic activity: To investigate the effect of water on condensation rates over CeO_2 catalysts, a series of reactions were conducted at 200 ˚C with varying amounts of water added into the system. Water was mixed with the solvent and catalyst before entering the reactant and starting the reaction. The detailed calculations of the states of water during reactions are included in **Section SIV** (**Supporting Information**). The enhancement of catalytic activity by water is estimated by comparing the reaction rate in the presence of water with the rate without added water: $Enhancement\ (\%) = \frac{r_w - r_{w/o}}{r_{w/o}} \times 100\ \%$

Measurement of active site density under reaction conditions by titration

Propionic acid and pyridine were used as titrants to assess the number of active surface sites involved in the aldol condensation of cyclopentanone. In these experiments, each liquid titrant was introduced into the system along with the reactant at the start of the reaction. As described in previous studies,[11, 22] propionic acid can irreversibly block acid-base site pairs, while pyridine selectively adsorbs on acid sites. The condensation rate should decrease when the site responsible for reactivity is blocked by the titrant. Accordingly, the amount of titrant required per unit catalyst mass to fully suppress the rate gives the density of active sites.

DFT calculations

The DFT calculations were performed using the Vienna ab initio simulation package (VASP). To accurately reproduce the electronic and structural properties of CeO_2, we conducted spin-polarized DFT+U calculations with a value of 5.0 eV applied to the Ce 4f states.[43-44] The Perdew-Burke-Ernzerhof (PBE) functional was used to describe the exchange correlation energy within the generalized gradient approximation (GGA).[45] The projector augmented wave (PAW) method was employed to describe the electron-ion interactions.[46-47] The cutoff energy of 400 eV was applied for the plane-wave basis set to represent valence electrons.[48] The DFT-D3 method was used for the correction of van der Waals interactions (vdW).[49] The electronic energies were converged within 10^{-5} eV, and the force on each atom was converged to below 0.02 eV.$Å^{-1}$.

Periodic CeO_2 (110), (100) and (111) slabs of a unit cell were constructed from DFT-derived CeO_2 bulk structures ($a = b = c$ = 0.540 nm). For the 2 × 1 CeO_2 (110) slab surface, 7 atomic layers with 13.3 Å thickness is used. For the 2 × 2 CeO_2 (100) slab surface, 9 atomic layers with 10.9 Å thickness is used. For this surface, it cannot be cut without leaving an excess of cations or anions, which creates a polar and unstable surface. The surface has been reconstructed by removal half of the oxygen atoms to overcome charge instability, as reported in previous study.[50] For the 2 × 2 CeO_2 (111) slab surface, 12 atomic layers with 10.5 Å thickness is used. The bottom two O-Ce-O layers were fixed at their bulk position while the top two O-Ce-O layers were allowed to relax in all optimizations. The 2 × 2 × 1 Monkhorst-pack k-point mesh was used to sample the first Brillouin zone. We checked that increasing the k-point to 4×4×1 wouldn't change the adsorption energy. The following discussion is thus only focused on calculation using 2×2×1. A vacuum layer of 20 Å along the *z*-direction was used.

The affinities of surfaces for NH_3 and BF_3 gases were used to probe Lewis acid-base properties of Ce-O pairs. NH_3 affinity (E_{NA}) for Lewis acid site (E_{Ce}) is defined as the energy release upon attachment of a gaseous NH_3 (E_{NH_3}) on to Ce center at the surface to form NH_3-Ce:

$$E_{NA} = E_{NH_3-Ce} - E_{NH_3} - E_{Ce}$$

Likewise, the BF_3 affinity (E_{BA}) for Lewis base site (E_O) can be defined as:

$$E_{BA} = E_{BF_3-O} - E_{BF_3} - E_O$$

The adsorption energy of CPO molecule on CeO_2 surfaces were defined as:

$$E_{CPO} = \frac{1}{2}(E_{(2CPO+surface)} - E_{surface} - 2E_{CPO})$$

Results and discussion

Atomic arrangement of CeO_2 nanoshapes with different surface terminations

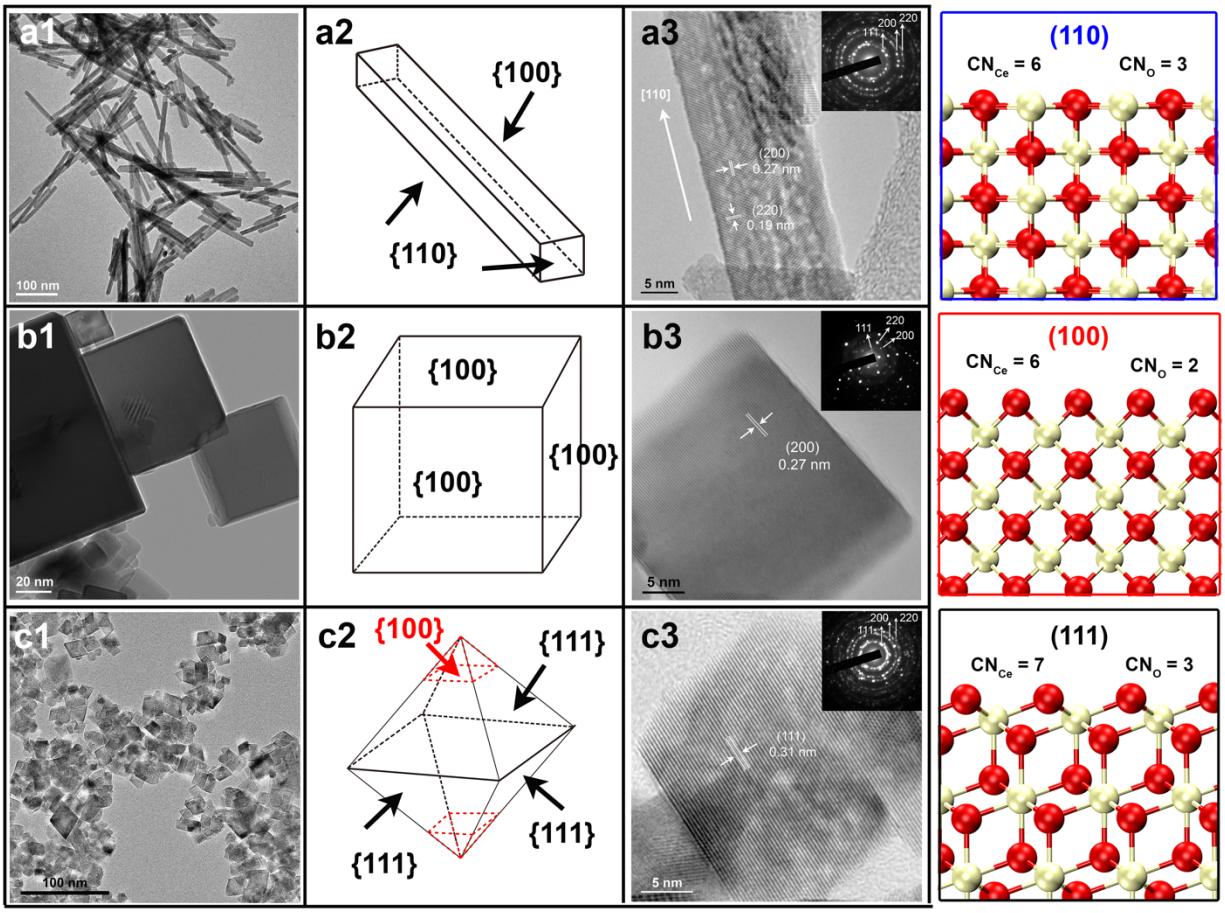

Figure 2. TEM and HRTEM images of CeO_2 nanorods (a), nanocubes (b) and octahedra (c) and schematic representation of CeO_2 facets (110), (100) and (111); Insets show the SAED patterns. Ce and O ions are represented by cream- and red-colored spheres.

Figure 2 and **Figure S1** show the TEM and HRTEM images for CeO_2 nanoshapes with rod-like, cubic and octahedral morphologies. It can be observed that CeO_2 nanorods are 10 nm in average diameter and 50–150 nm in length. The simultaneous presence of (200) and (220) surface-termination planes on these nanoparticles was identified by HRTEM, which corroborated the expected interplanar spacings of 0.27 and 0.19 nm, respectively. By contrast, the 50 nm CeO_2 nanocubes only exhibited the presence of (200) planes. Finally, the CeO_2 octahedra showed a uniform particle size of ~ 20 nm, exposing predominantly (111) planes. The selected-area electron

diffraction (SAED) patterns verify the single-crystal nature of the CeO_2 nanocubes and the polycrystallinity of the CeO_2 rod-like and octahedral nanoparticles.

X-ray diffraction patterns of the nanoshaped ceria are summarized in **Figure S2**. All the diffraction peaks can be assigned to cubic fluorite CeO_2 (JCPDF04-0593, space group $Fm\bar{3}m$). The peak intensities of the CeO_2 nanocubes reflect their high crystallinity and the similarity between the average particle size determined from Debye-Scherrer equation and that measured from TEM further validates the single-crystal nature of this sample. By contrast, for the nanorods and octahedra the crystal size values estimated from the same XRD method are much smaller than those observed by TEM. Accordingly, as summarized in **Table S1**, the nanorods and octahedra show relatively higher surface area than nanocubes. The slight lattice expansion of nanorods compared to bulk values indicates the presence of a significant density of defects, associated to the formation of oxygen vacancies. Indeed, as shown in the **Figure S4** and **Table S3**, XPS experiments confirm a lower O fraction and a higher density of Ce^{3+} species on the surface of this sample, consistent with a higher density of O vacancies, since each one of them generates two Ce^{3+} cations.

Interestingly, on the nanocubes sample, XPS gave evidence for the presence of a significant concentration of Na, which was absent on the other two samples. As proposed in previous studies, Na impurities might influence the acid-base properties of CeO_2 and affect its reactivity.[41, 51-52] Therefore, to explore the potential role of Na, we have treated these CeO_2 nanocubes to minimize the Na content and determine the effects of this removal on catalytic activity and selectivity. A previously described acid-base washing process was employed for this purpose.[41] As shown in **Figure S6**, XPS demonstrates the complete elimination of Na species. Nevertheless, a direct comparison of the catalytic activity of the nanocube samples with or without Na showed minimal differences in rate and product distribution. Moreover, of greater importance in our study, the reaction kinetics for the CeO_2 nanocubes did not change by the presence of Na species (see **section SII, supporting information**). Therefore, in the rest of the study, we have focused on the analysis of the nanocube catalysts without the acid-base treatment.

Figure 2 illustrates the atomic arrangement of three low-index CeO_2 facets (110), (100) and (111), which corresponds to the predominant surface terminations of nanorods, nanocubes and octahedra, respectively. For the (110) surface each atomic layer contains a stoichiometric amount of Ce and O species, making it charge balanced at the surface. As a result, the surface of this plane

is nonpolar. By contrast, each atomic plane for the (100) and (111) surfaces is terminated with either Ce cations or O anions. When the surface layer of (100) plane is terminated by O, the Ce layer underneath is not easily accessible to gas phase. This surface is rather unstable and tends to undergo reconstruction in which a fraction of the O atoms from the top layer are removed, as shown by scanning tunneling microscope (STM) and rationalized by DFT calculations.[50, 53] Finally, the (111) plane has an open structure with a O-Ce-O trilayer that repeats along the surface. As a result, the coordination numbers of surface Ce (CN_{Ce}) for (110), (100) and (111) planes are 6, 6, and 7, while the coordination numbers for O (CN_O) are 3, 2, and 3, respectively.

Quantification of acid-base pairs of CeO_2 nanoshapes by in situ titration method

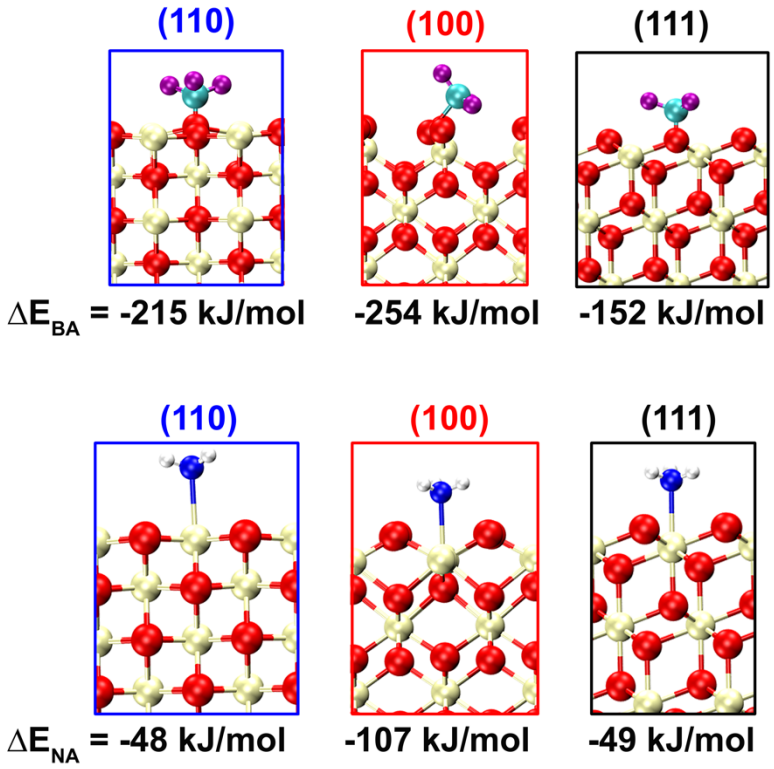

Figure 3. DFT calculations of BF_3 (ΔE_{BA}) and NH_3 (ΔE_{NA}) adsorption on CeO_2 surfaces. Red: O anions; Cream: Ce cations; Silver: C; White: H; Blue: N; Cyan: B; Purple: F. The adsorption values are labelled below each structure.

It is well-accepted that the acid-base properties of metal oxides are related to the coordination number of each species on the surface. To investigate the acid-base characteristics of the different

CeO_2 nanoshaped-crystals, conventional CO_2-TPD experiments were performed. As shown in **Figure S5**, the density of basic sites clearly ranks in the order nanorods > nanocubes > octahedra. However, the differences in basicity strength for the different samples are not obvious. Therefore, we have conducted DFT calculations for the affinity of BF_3 and NH_3, to quantify the basicity and acidity strengths, respectively. As shown in **Figure 3**, the basicity strength is higher than the acidity strength on the three CeO_2 crystal planes. The basicity, derived from the adsorption of BF_3 on O atoms, follows the order (100) > (110) > (111). Accordingly, we could expect that the basicity strength on the nanoparticles will follow the trend nanocubes > nanorods > octahedra. However, as shown below, the observed intrinsic activity does not follow this trend.

In addition, due to the weak interaction of CO_2 on the ceria surface, a large fraction of CO_2 desorbs at room temperature under He flow.[12, 41] Therefore, the density of basic sites measured from CO_2-TPD is much lower than the expected theoretical value, as shown in **Table S5**. In recent years, in-situ titration by probe molecules that irreversibly bind to active sites and cause a one-to-one deactivation has been used as an effective method for quantifying the number of sites under reaction conditions.[22] By using this titration method, one can obtain direct comparisons of turnover frequencies on different samples.[11-12, 14]

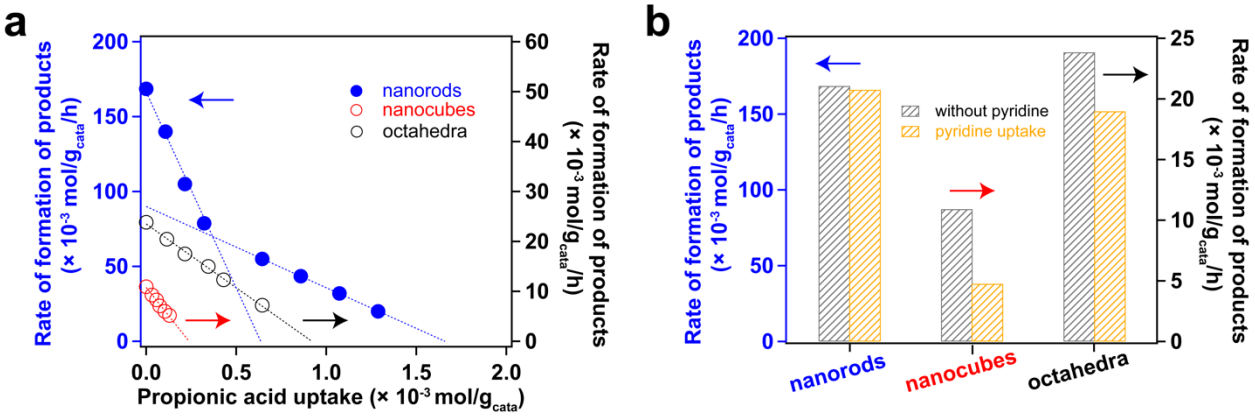

Figure 4. (a) Cyclopentanone condensation rates on CeO_2 nanoshapes as a function of propionic acid addition; (b) Cyclopentanone condensation rates on CeO_2 nanoshapes with introducing of 0.08×10^{-3} mol/g_{cata} pyridine.

Propionic acid is an effective titrating agent for acid-base pair sites, while pyridine can selectively bind to Lewis acid sites. As shown in **Figure 4a**, when the site titration was performed on the nanocubes and octahedra a linear drop in rate was obtained. If one extrapolates this line to

zero rate, the interception with the X-axis yields the total number of sites. Therefore, the ratio of maximum rate per unit mass observed without titrant to the total number of sites per unit mass yields the TOF. By contrast, two linear regions were obtained with the nanorods. The first linear drop extrapolated to zero rate yields a site density of 0.64×10^{-3} mol/g_{cata}, while the other trend with a smaller slope yields a second site density of 1.65×10^{-3} mol/g_{cata}. This behavior could be ascribed to the presence of active sites of different activity and basic strength.[24] The linearity of both trends would indicate that the stronger basic sites, with higher activity, are titrated first by propionic acid, while those of lower activity and weaker basicity are titrated later. The sum of the two types of sites estimated from these titration measurements is in good agreement with the calculate density of sites for the corresponding planes, as summarized in **Table S5.** The agreement is also good for the other nanoparticles, with a slightly lower density of basic sites obtained for the nanocubes, which can be ascribed to the reconstruction of the (100) surface described above. In summary, this method not only gives a more consistent trend of number of sites than that obtained from CO_2-TPD (see for example **Figure S5 and Figure 4a)** but it measures density of sites under reaction conditions.

Relationship between structure and reactivity of CeO_2 nanoshapes

Table 1 Catalytic activity of CeO_2 catalysts with different shapes.

Catalysts	Reaction rate ($\times 10^{-3}$ mol/g_{cata}/h)	Acid-base density ($\times 10^{-3}$ mol/g_{cata})[b]	TOF (h^{-1})
CeO_2 nanorods	168.5	0.64	263.3
	90.0[a]	1.01	89.1
CeO_2 nanocubes	10.9	0.24	45.8
CeO_2 octahedra	23.9	0.90	26.6

[a] Rate estimated from in situ titration (see **Figure 4a**) as the intercept for the line with the lower slope;

[b] Density measured by the in situ titration method, extrapolating to zero rate.

Table 1 shows the catalytic activity of the three CeO_2 nanoshapes. Among them, the CeO_2 nanorods exhibit the highest catalytic activity. Both, CeO_2 nanocubes and octahedra show lower

activity. While the latter shows a higher rate per mass than the former, the opposite is true with the TOF values.

Next, kinetics experiments were performed to rationalize the remarkably different catalytic activity of these CeO_2 nanoshapes. **Figure 5** compares the initial rates on CeO_2 nanoshapes with respect to the CPO concentration. In the low concentration range (0.0-0.5 M CPO, **Figure 5a**), the initial rate on CeO_2 nanorods increases linearly with CPO concentration, indicating a first-order behavior. By contrast, parabolic curves with a slope of zero at zero concentration were observed for both CeO_2 nanocubes and octahedra, which corresponds to second-order dependence.

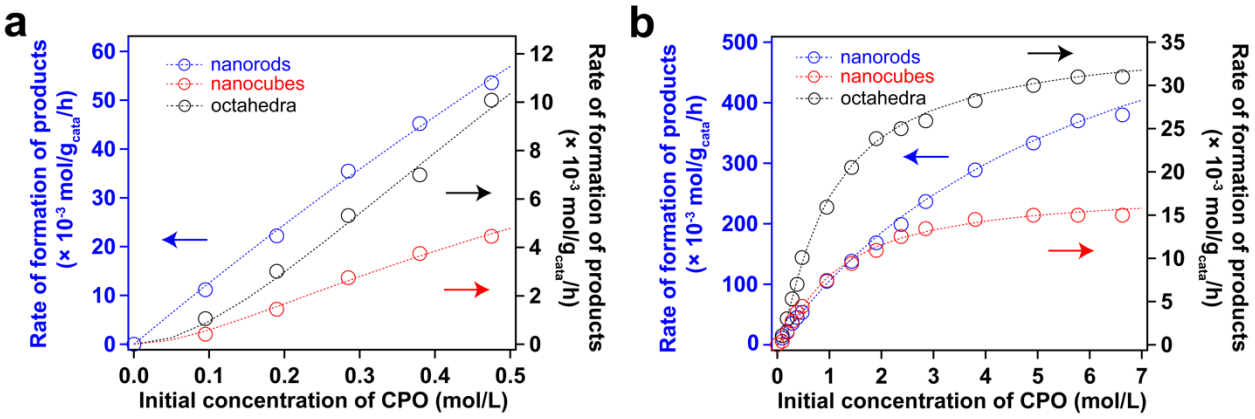

Figure 5. Cyclopentanone condensation rates on CeO_2 nanoshapes with respect to the initial concentration of cyclopentanone. Symbols are observed data; dash lines are fitted curve by L-H reaction model.

The elementary steps of aldol condensation reaction include the adsorption of reactant, α-C–H abstraction to form enolate species, nucleophilic addition between enolate and another CPO molecule (C–C coupling), reprotonation, dehydration of aldol product and desorption of water and unsaturated ketones. Among these steps, enolate formation should follow a first-order kinetics with respect to the surface concentration, while C–C coupling should be second-order.[22]

Both, the high TOF and the first order kinetics observed on CeO_2 nanorods indicate that the bimolecular C–C coupling is fast on this catalyst and the formation of enolate species is the rate-limiting step. Contrary, on the CeO_2 nanocubes and octahedra, the TOF values are relatively low and the kinetics is second order, which is consistent with a slower rate of C–C coupling. As shown in the **supporting information**, if a step following the C–C coupling such as reprotonation (or

desorption) of the dimer were rate limiting, the reaction order would also be second. However, if that were the case, the rate would be lower for the catalyst with the higher basicity (i.e. nanocubes) since it would make the proton transfer (or desorption) more difficult. However, this would be the opposite trend as that shown in **Table 1**. Therefore, being the C–C coupling step rate-limiting, one can consider two possible alternatives for this step.

That is, the enolate formed in the first step can either react with another CPO molecule from the liquid phase (Eley-Rideal model, E-R) or with an adsorbed CPO molecule (Langmuir-Hinshelwood model, L-H). At high enough CPO concentrations, it is observed that the rate curves start plateauing (Figure 5b), which is the typical behavior for L-H kinetics. By contrast, for E-R kinetics the rate would continue increasing as full coverage is approached. Both, nonlinear and linear regressions only show excellent fittings for all three CeO_2 nanoshapes with the L-H model, which further validates the proposed reaction mechanism (see **Figure 5b** and **Figure 6**).

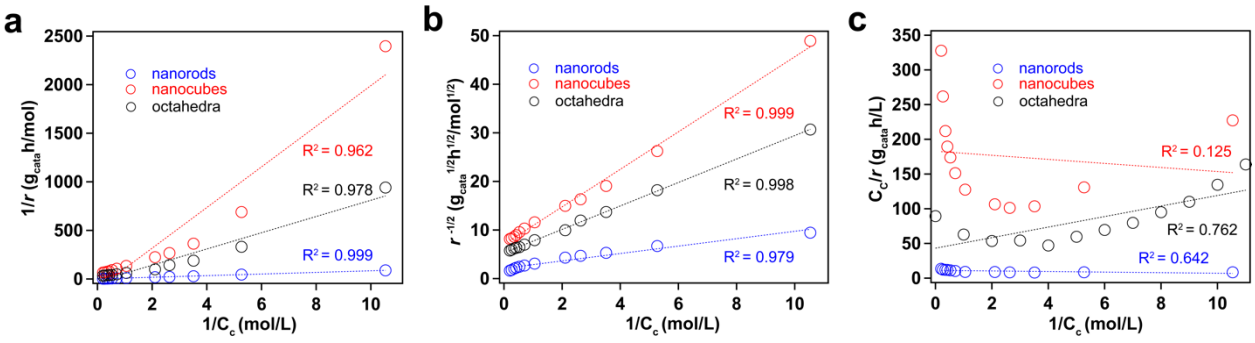

Figure 6. Linearization of reaction models on CeO_2 catalysts: (a) first-order L-H model; (b) second-order L-H model; (c) second-order E-R model.

In the mechanism in which the bimolecular surface reaction is the rate limiting step (on nanocubes and octahedra), the polarized carbonyl C bound to a Lewis acid site undergoes a nucleophilic attack by the enolate species activated at a vicinal site. Therefore, when pyridine is added during reaction (**Figure 4b**), the interaction between pyridine and the acid sites inhibits the polarization of carbonyl and lowers the C–C coupling rates. By contrast, pyridine does not affect the condensation rate on CeO_2 nanorods, which is not limited by the bimolecular C–C coupling step.

In a recent study on ketonization of carboxylic acids, it has been proposed that the stronger basic sites favor the formation of more stable enolate species on the surface via a stronger stabilization of the α-C–H atom, which in turn may lower the activation barrier for C–C bond formation.[48] Therefore, when comparing the activity of nanocubes and octahedra catalysts, for which the reaction is limited by C–C bond formation, it is conceivable that the relatively stronger basicity of nanocubes may be responsible for its higher catalytic activity. That is, the catalytic activity of the different CeO_2 nanoshapes: nanorods > nanocubes > octahedra may be a combination of both topological and acid/base properties.

Different arrangements of surface atoms result in different reaction kinetics

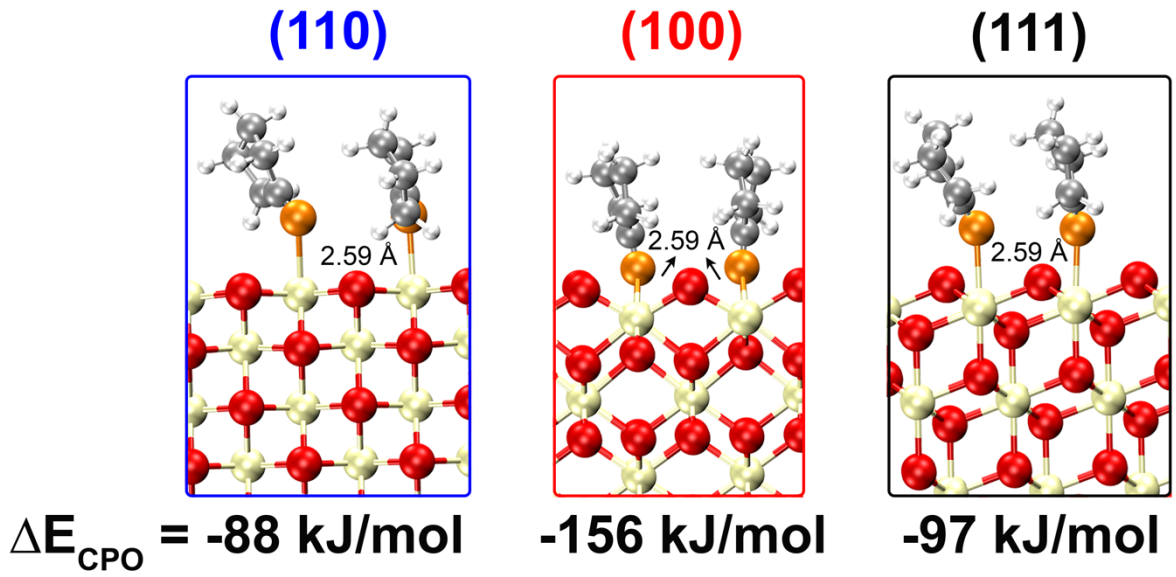

Figure 7. Adsorption of CPO molecules on CeO_2 crystal planes. The Ce, O, C, H are cream, red, silver and white, respectively. The carbonyl O is indicated with orange color. The Ce-O (carbonyl) bond length at the interface is labelled.

Figure 7 illustrates the interactions of two CPO molecules with the different CeO_2 surfaces. The bond lengths between Ce cations and lattice O anions are all the same (2.34 Å) for the three surfaces. Therefore, it can be concluded that the different reaction kinetics observed on these

surfaces is not caused by differences in the cation-oxygen distance. This was the case for TiO_2-catalyzed aldol condensation reaction,[22] but it does not seem to be the crucial effect for these ceria catalysts.

When CPO interacts with a Lewis acid site on the CeO_2 surface, the O atom of the carbonyl is polarized, which causes the weakening the C=O bond. However, the same Ce-O bond length (2.59 Å) between the Ce site and the O of the carbonyl is observed on the three different crystal planes, indicating a similar extent of polarization. Moreover, the C=O bond length is the same on all three surfaces (1.24 Å), but longer than that in the gas phase CPO (1.22 Å).

Nevertheless, a wide range of adsorption strengths is observed on the three surfaces. While the interaction with the flat (110) surface is not significantly strong (-88 kJ/mol), the first O atomic layer protruding on the surfaces of (100) and (111) planes strongly enhance the interaction, particularly for the (100) surface, for which the adsorption energy is -156 kJ/mol. Interestingly, while this oxygen layer enhances the strength of adsorption, it interferes between adsorbates on contiguous Ce sites, which hinders the approach of the enolate to the second molecule in the C–C coupling step, leading to the observed second order behavior for nanocubes (100) and octahedra (111). By contrast, the uniform surface arrangement of Ce and O atoms on the (110) plane of nanorods facilitates the C–C coupling, making α-C–H abstraction rate limiting. In summary, the activity of CeO_2-catalyzed aldol condensation is shape-dependent due to the different atomic arrangement of the terminated surfaces, which leads to different reaction mechanisms.

Water promotes the C–C coupling step via remote bond polarization

In aldol condensation, water is present as a by-product (or added in the feed) and can be either an inhibitor of the α-C–H abstraction step or a promoter of the C–C coupling step.[11, 14] **Figure 8** shows the rate of CPO aldol condensation on CeO_2 nanoshapes as a function of the amount water added, which can be reported as a ratio relative to the amount of water need to reach saturation under reaction conditions (see **Section SIV, Supporting Information**). **Table S12** compares the amount of water in situ formed during the condensation reactions and externally added. The water formed on all the three catalysts are much lower than the amount needed to reach saturation.

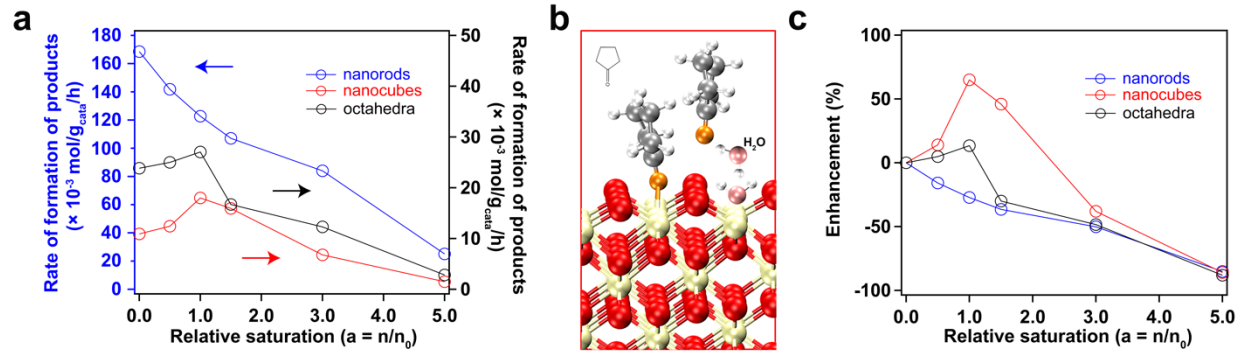

Figure 8. (a) Rate of formation of products with respect to the relative saturation; (b) Illustration of water bridge between Ce cation on (100) surface and adsorbed CPO molecule; The Ce, O, C, H are cream, red, silver and white, respectively; the carbonyl O is labeled as orange color; the O for H_2O molecules are labeled as pink color; (c) Percent enhancement by water addition on CeO_2 nanoshapes relative to the water-free rate.

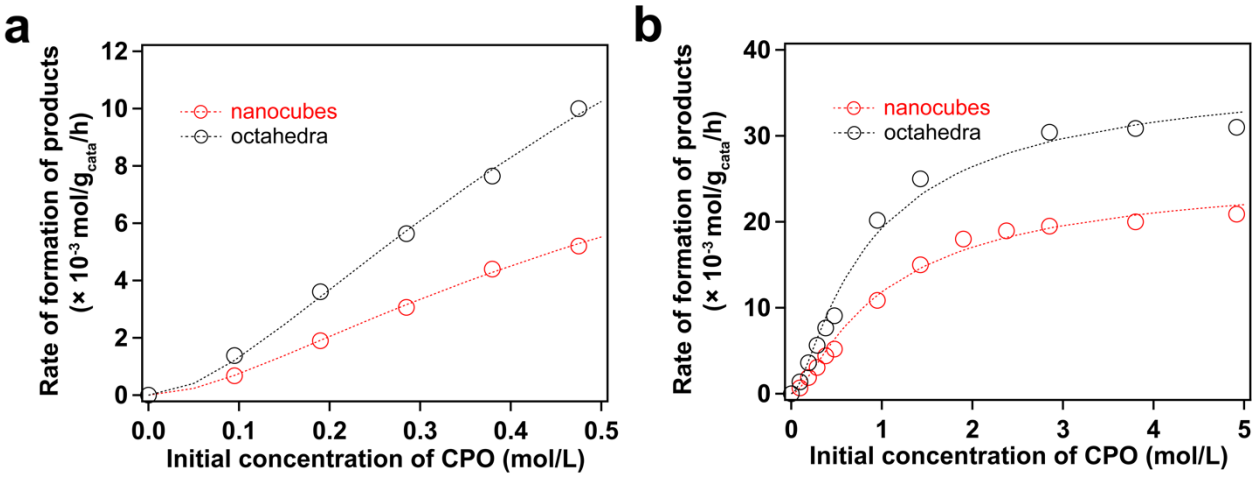

Figure 9. Initial rates of formation of products over CeO_2 catalysts as a function of cyclopenatnone concentration in the presence of water. The amount of water added is 0.2 mL ($n/n_0 \approx 1$). Symbols are observed data; dash lines are fitted curve by L-H reaction model.

It can be observed that, on CeO_2 nanorods, the condensation rate continuously decreases with the addition of water. By contrast, CeO_2 nanocubes and octahedra show significant enhancement in catalytic activity when water is added. **Figure 8c** compares to the condensation rates on the three nanoshapes relative to those obtained under water-free conditions and shows that the condensation rates increase up to 65 and 15 % on CeO_2 nanocubes and octahedra, respectively, when the amount of added water starts condensing ($n/n_0 \approx 1$). Kinetics analysis shows that water does not change the reaction kinetics on CeO_2 nanocubes and octahedra, with the C–C coupling

step remaining as rate-limiting (see **Figure 9 and 10**). Therefore, we propose that on these surfaces water enhances the CPO aldol condensation on CeO_2 nanocubes and octahedra by "remote bond polarization." [39]

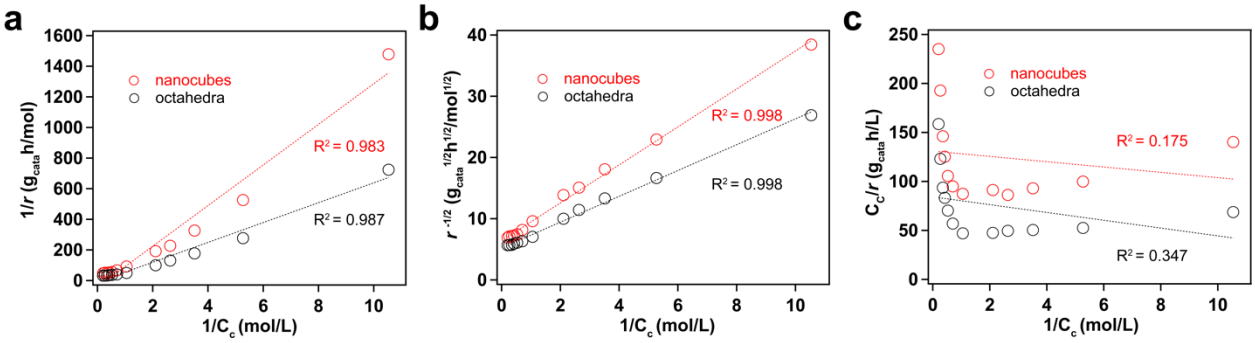

Figure 10. Linearization of reaction models on CeO_2 catalysts in the presence of water: (a) first-order L-H model; (b) second-order L-H model; (c) second-order E-R model.

The spatial hindrance between enolate species and polarized CPO molecules is overcome by formation of a water chain between the CPO molecule nearby the enolate species and the Lewis acid site which acts as a bond polarizer to enhance electrophilicity of the electron accepting adsorbate (see **Figure 8b**). In this way, the water chain acts as a molecular bridge to transfer the polarization from the Lewis acid site to the C=O bond of the CPO molecule, accelerating the rate limiting C–C coupling step. By contrast, the first order reaction on nanorods is not promoted, but rather inhibited by the presence of water due to the site blockage caused by water competitive adsorption.

Conclusions

Well-defined ceria nanoshapes can be used to conduct kinetics studies on preferential crystal planes and provide a general platform for direct identification and quantification of active sites under realistic reaction conditions. These studies have allowed us to obtain relationships between topological characteristics of metal oxides and their catalytic performance for condensation reactions. The major conclusions are:

(a) The catalytic activity of CeO_2 nanoshapes for aldol condensation of cyclopentanone follows the order: nanorods > nanocubes > octahedra.

(b) The catalytic performance of nanoshapes is determined not only by the acid-base properties, but also by the surface topology of the specific exposed facets.

(c) On nanorods, the reaction is limited by α-C–H abstraction since the flat atomic surface of the prevailing (110) plane facilitates the C–C coupling. On these catalysts, the addition of water results in rate inhibition by site blocking.

(d) Nanocubes and octahedra, containing (100) and (111) planes, respectively, have a rougher surface with an upper O layer that interferes between adsorbate-adsorbate interactions and makes C–C coupling more difficult. Therefore, C–C bond formation becomes rate limiting on nanocubes and octahedra. On these surfaces, the presence of water helps overcoming the spatial hindrance caused by the rough atomic arrangement and speeds-up the rate-limiting C–C coupling step by remote bond polarization.

Supporting information

The Supporting information is available free of charge. The file includes characterization of CeO_2 nanoshapes; study of the effect of Na impurities on aldol condensation reaction catalyzed by CeO_2 nanocubes; details of the reaction kinetics fitting and the study of the effect of water on the condensation reaction.

Author information

Corresponding Author*

D.E. Resasco (resasco@ou.edu)

Notes

The authors have no competing interests to disclose.

Acknowledgements

This work was supported by the U.S. Department of Energy, Office of Science, Basic Energy Sciences under Award Number DE-SC0018284. The computational research used supercomputer

resource of OU Supercomputing Center for Education & Research (OSCER) at the University of Oklahoma.

References:

1. Randery, S. D.; Warren, J. S.; Dooley, K. M., Cerium Oxide-Based Catalysts for Production of Ketones by Acid Condensation. *Appl. Catal., A* **2002,** *226*, 265–280.
2. Nagashima, O.; Sato, S.; Takahashi, R.; Sodesawa, T., Ketonization of Carboxylic Acids Over CeO_2-based Composite Oxides. *J. Mol. Catal. A: Chem.* **2005,** *227*, 231–239.
3. Simon, I.; Bârsan, N.; Bauer, M.; Weimar, U., Micromachined Metal Oxide Gas Sensors: Opportunities to Improve Sensor Performance. *Sens. Actuators, B* **2001,** *73*, 1–26.
4. Su, J.; Cao, L.; Li, L.; Wei, J.; Li, G.; Yuan, Y., Highly Sensitive Methane Catalytic Combustion Micro-Sensor Based On Mesoporous Structure and Nano-catalyst. *Nanoscale* **2013,** *5*, 9720–9725.
5. Ormerod, R. M., Solid Oxide Fuel Cells. *Chem. Soc. Rev.* **2003,** *32*, 17–28.
6. Li, W.; Liu, J.; Zhao, D., Mesoporous Materials for Energy Conversion and Storage Devices. *Nat. Rev. Mater.* **2016,** *1*, 1–17.
7. Wei, J.; Sun, Z.; Luo, W.; Li, Y.; Elzatahry, A. A.; Al-Enizi, A. M.; Deng, Y.; Zhao, D., New Insight into the Synthesis of Large-Pore Ordered Mesoporous Materials. *J. Am. Chem. Soc.* **2017,** *139*, 1706–1713.
8. Jo, C.; Hwang, J.; Lim, W. G.; Lim, J.; Hur, K.; Lee, J., Multiscale Phase Separations for Hierarchically Ordered Macro/Mesostructured Metal Oxides. *Adv. Mater.* **2018,** *30*, 1703829.
9. Vivier, L.; Duprez, D., Ceria-Based Solid Catalysts for Organic Chemistry. *ChemSusChem* **2010,** *3*, 654–678.
10. Ngo, D. T.; Sooknoi, T.; Resasco, D. E., Improving Stability of Cyclopentanone Aldol Condensation MgO-Based Catalysts by Surface Hydrophobization with Organosilanes. *Appl. Catal., B* **2018,** *237*, 835–843.
11. Ngo, D. T.; Tan, Q.; Wang, B.; Resasco, D. E., Aldol Condensation of Cyclopentanone on Hydrophobized MgO. Promotional Role of Water and Changes in the Rate-Limiting Step upon Organosilane Functionalization. *ACS Catal.* **2019,** *9*, 2831–2841.
12. Li, G.; Dissanayake, S.; Suib, S. L.; Resasco, D. E., Activity and Stability of Mesoporous CeO_2 and ZrO_2 Catalysts for the Self-Condensation of Cyclopentanone. *Appl. Catal., B.* **2020**, *267*, 118373.
13. Collier, V. E.; Ellebracht, N. C.; Lindy, G. I.; Moschetta, E. G.; Jones, C. W., Kinetic and Mechanistic Examination of Acid–Base Bifunctional Aminosilica Catalysts in Aldol and Nitroaldol Condensations. *ACS Catal.* **2015,** *6*, 460–468.
14. Li, G.; Wang, B.; Chen, B.; Resasco, D. E., Role of Water in Cyclopentanone Self-Condensation Reaction Catalyzed by MCM-41 Functionalized with Sulfonic Acid Groups. *J. Catal.* **2019,** *377*, 245–254.
15. Nikolopoulos, A.; Jang, B.-L.; Spivey, J., Acetone Condensation and Selective Hydrogenation to MIBK on Pd and Pt Hydrotalcite-Derived MgAl Mixed Oxide Catalysts. *Appl. Catal., A* **2005,** *296*, 128–136.
16. Di Cosimo, J. I.; Torres, G.; Apesteguıa, C., One-Step MIBK Synthesis: A New Process From 2-propanol. *J. Catal.* **2002,** *208*, 114–123.
17. Hakim, S. H.; Shanks, B. H.; Dumesic, J. A., Catalytic Upgrading of the Light Fraction of A Simulated Bio-Oil Over $CeZrO_x$ Catalyst. *Appl. Catal., B* **2013,** *142*, 368–376.

18. Young, Z. D.; Hanspal, S.; Davis, R. J., Aldol Condensation of Acetaldehyde Over Titania, Hydroxyapatite, and Magnesia. *ACS Catal.* **2016,** *6*, 3193–3202.
19. Wang, S.; Iglesia, E., Substituent Effects and Molecular Descriptors of Reactivity in Condensation and Esterification Reactions of Oxygenates on Acid–Base Pairs at TiO_2 and ZrO_2 Surfaces. *J. Phys. Chem. C* **2016,** *120*, 21589–21616.
20. Resasco, D. E.; Wang, B.; Crossley, S., Zeolite-Catalysed C–C Bond Forming Reactions for Biomass Conversion to Fuels and Chemicals. *Catal. Sci. Tech.* **2016,** *6*, 2543–2559.
21. Resasco, D. E.; Wang, B.; Sabatini, D., Distributed Processes for Biomass Conversion Could Aid UN Sustainable Development Goals. *Nat. Catal.* **2018,** *1*, 731–735.
22. Wang, S.; Goulas, K.; Iglesia, E., Condensation and Esterification Reactions of Alkanals, Alkanones, and Alkanols on TiO_2: Elementary Steps, Site Requirements, and Synergistic Effects of Bifunctional Strategies. *J. Catal.* **2016,** *340*, 302–320.
23. Idriss, H.; Barteau, M. A., Active Sites on Oxides: From Single Crystals to Catalysts. *Adv. Catal.* **2000**, *45*, 261–331.
24. Sherrill, A.; Idriss, H.; Barteau, M.; Chen, J., Adsorption and Reaction of Acrolein on Titanium Oxide Single Crystal Surfaces: Coupling Versus Condensation. *Catal. Today* **2003,** *85*, 321–331.
25. Mullins, D. R., The Surface Chemistry of Cerium Oxide. *Surf. Sci. Rep.* **2015,** *70*, 42-85.
26. Idriss, H.; Kim, K.; Barteau, M., Carbon–Carbon Bond Formation via Aldolization of Acetaldehyde on Single Crystal and Polycrystalline TiO_2 Surfaces. *J. Catal.* **1993,** *139*, 119–133.
27. Benz, L.; Haubrich, J.; Quiller, R. G.; Jensen, S. C.; Friend, C. M., McMurry Chemistry on TiO_2 (110): Reductive C–C Coupling of Benzaldehyde Driven by Titanium Interstitials. *J. Am. Chem. Soc.* **2009,** *131*, 15026–15031.
28. Shen, M.; Zaera, F., Coupling Reactions in Aldehydes Adsorbed on V (100) Single-Crystal Surfaces. *J. Am. Chem. Soc.* **2009,** *131*, 8708–8713.
29. Benz, L.; Haubrich, J.; Quiller, R. G.; Friend, C. M., Acrolein Coupling on Reduced TiO_2 (110): The Effect of Surface Oxidation and The Role of Subsurface Defects. *Surf. Sci.* **2009,** *603*, 1010–1017.
30. Li, G.; Li, L.; Yuan, Y.; Shi, J.; Yuan, Y.; Li, Y.; Zhao, W.; Shi, J., Highly Efficient Mesoporous Pd/CeO_2 Catalyst for Low Temperature CO Oxidation Especially Under Moisture Condition. *Appl. Catal., B* **2014,** *158*, 341–347.
31. Liu, J.; Zhao, Z.; Xu, C.; Liu, J., Structure, Synthesis, and Catalytic Properties of Nanosize Cerium-Zirconium-Based Solid Solutions in Environmental Catalysis. *Chin. J. Catal.* **2019,** *40* (10), 1438–1487.
32. Wu, Z.; Li, M.; Overbury, S. H., On The Structure Dependence of CO Oxidation Over CeO_2 Nanocrystals With Well-Defined Surface Planes. *J. Catal.* **2012,** *285*, 61–73.
33. Li, G.; Wu, B.; Li, L., Surface-Structure Effect of Nano-Crystalline CeO_2 Support on Low Temperature CO oxidation. *J. Mol. Catal. A: Chem.* **2016,** *424*, 304–310.
34. Kamimura, Y.; Sato, S.; Takahashi, R.; Sodesawa, T.; Akashi, T., Synthesis of 3-pentanone From 1-propanol Over CeO_2–Fe_2O_3 Catalysts. *Appl. Catal., A* **2003,** *252*, 399–410.
35. Huang, P.; Wu, F.; Zhu, B.; Gao, X.; Zhu, H.; Yan, T.; Huang, W.; Wu, S.; Song, D., CeO_2 Nanorods and Gold Nanocrystals Supported on CeO_2 Nanorods As Catalyst. *J. Phys. Chem. B* **2005,** *109* (41), 19169–19174.
36. Campo, B.; Volpe, M.; Ivanova, S.; Touroude, R., Selective Hydrogenation of Crotonaldehyde on Au/HSA-CeO_2 Catalysts. *J. Catal.* **2006,** *242*, 162–171.

37. Raskó, J.; Kiss, J., Adsorption and Surface Reactions of Acetaldehyde on TiO_2, CeO_2 and Al_2O_3. *Appl. Catal., A.* **2005,** *287*, 252–260.
38. Mann, A. K.; Wu, Z.; Calaza, F. C.; Overbury, S. H., Adsorption and Reaction of Acetaldehyde on Shape-Controlled CeO_2 Nanocrystals: Elucidation of Structure–Function Relationships. *ACS Catal.* **2014,** *4*, 2437–2448.
39. Li, G.; Wang, B.; Resasco, D. E., Water-Mediated Heterogeneously Catalyzed Reactions. *ACS Catal.* **2020,** *10*, 1294–1309.
40. Hronec, M.; Fulajtarová, K., Selective Transformation of Furfural to Cyclopentanone. *Catal. Commun.* **2012,** *24*, 100–104.
41. Wu, Z.; Mann, A. K.; Li, M.; Overbury, S. H., Spectroscopic Investigation of Surface-Dependent Acid–Base Property of Ceria Nanoshapes. *J. Phys. Chem. C* **2015,** *119*, 7340–7350.
42. Mai, H.-X.; Sun, L.-D.; Zhang, Y.-W.; Si, R.; Feng, W.; Zhang, H.-P.; Liu, H.-C.; Yan, C.-H., Shape-Selective Synthesis and Oxygen Storage Behavior of Ceria Nanopolyhedra, Nanorods, and Nanocubes. *J. Phys. Chem. B* **2005,** *109*, 24380–24385.
43. Nolan, M., Enhanced Oxygen Vacancy Formation in Ceria (111) and (110) Surfaces Doped With Divalent Cations. *J. Mater. Chem.* **2011,** *21*, 9160–9168.
44. Nolan, M.; Parker, S. C.; Watson, G. W., The Electronic Structure of Oxygen Vacancy Defects at The Low Index Surfaces of Ceria. *Surf. Sci.* **2005,** *595*, 223–232.
45. Perdew, J. P.; Burke, K.; Ernzerhof, M., Generalized Gradient Approximation Made Simple. *Phys. Rev. Lett.* **1996,** *77*, 3865.
46. Blöchl, P. E., Projector Augmented-Wave Method. *Phys. Rev. B* **1994,** *50*, 17953.
47. Kresse, G.; Joubert, D., From Ultrasoft Pseudopotentials to The Projector Augmented-Wave Method. *Phys. Rev. B* **1999,** *59*, 1758.
48. Wang, S.; Iglesia, E., Experimental and Theoretical Evidence for the Reactivity of Bound Intermediates in Ketonization of Carboxylic Acids and Consequences of Acid–Base Properties of Oxide Catalysts. *J. Phys. Chem. C* **2017,** *121*, 18030–18046.
49. Grimme, S.; Antony, J.; Ehrlich, S.; Krieg, H., A Consistent and Accurate Ab Initio Parametrization of Density Functional Dispersion Correction (DFT-D) For The 94 Elements H-Pu. *J. Chem. Phys.* **2010,** *132*, 154104.
50. Nörenberg, H.; Harding, J., The Surface Structure of CeO_2 (001) Single Crystals Studied by Elevated Temperature STM. *Surf. Sci.* **2001,** *477*, 17–24.
51. Gines, M. J.; Iglesia, E., Bifunctional Condensation Reactions of Alcohols on Basic Oxides Modified by Copper and Potassium. *J. Catal.* **1998,** *176*, 155–172.
52. Wang, Y.; Wang, F.; Song, Q.; Xin, Q.; Xu, S.; Xu, J., Heterogeneous Ceria Catalyst With Water-Tolerant Lewis Acidic Sites For One-Pot Synthesis of 1, 3-diols via Prins Condensation and Hydrolysis Reactions. *J. Am. Chem. Soc.* **2013,** *135*, 1506–1515.
53. Baudin, M.; Wójcik, M.; Hermansson, K., Dynamics, Structure and Energetics of The (111), (011) and (001) Surfaces of Ceria. *Surf. Sci.* **2000,** *468*, 51–61.

Table of contents

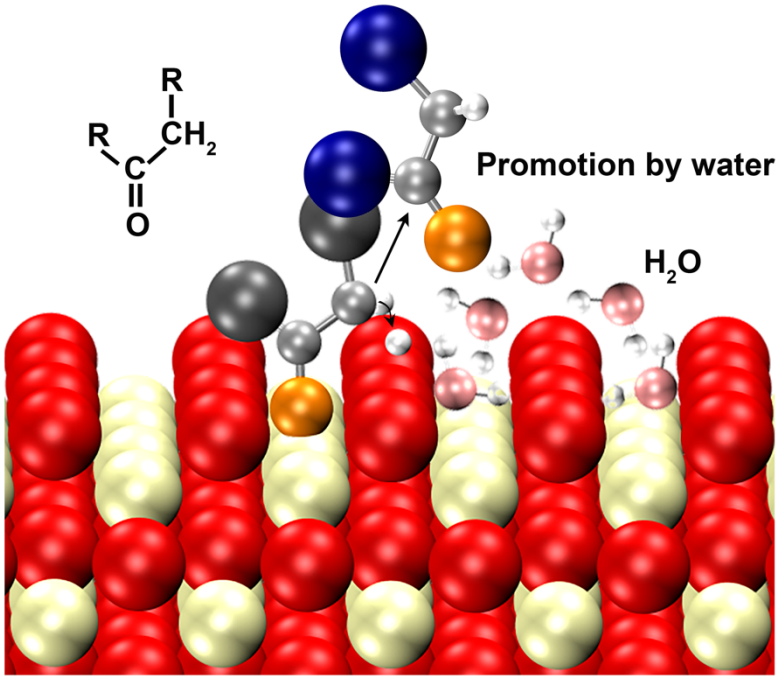

Remote bond Polarization